Universal depletion of metal-poor globular clusters in inner galaxy regions: Fossil record of black hole retention

Ali Rostami-Shirazi^{1*}, Narges Rostami², Hosein Haghi^{1,3,4}, and Akram Hasani Zonoozi^{3,4}

- School of Astronomy, Institute for Research in Fundamental Sciences (IPM), PO Box 19395-5531, Tehran, Iran
- Department of Physics, Faculty of Physics, Alzahra University, Vanak, 1993891176, Tehran, Iran
- Department of Physics, Institute for Advanced Studies in Basic Sciences (IASBS), 444 Prof. Sobouti Blvd., Zanjan 45137-66731,
- Helmholtz-Institut für Strahlen-und Kernphysik (HISKP), Universität Bonn, Nussallee 14-16, D-53115 Bonn, Germany

ABSTRACT

We analyzed the spatial distribution of globular cluster (GC) systems across 37 host galaxies in a two-dimensional parameter space defined by projected galactocentric distances (Rg) and metallicity ([Fe/H]). We identified a universal triangular depleted region, characterized by a lack of metal-poor GCs in the inner parts of host galaxies. The morphology of this depleted region correlates with the luminous mass of host galaxies; more massive galaxies consistently exhibit more extended depleted regions. We attribute this phenomenon to the combined influence of large-scale galactic assembly and internal GC dynamics, particularly the initial retention of black holes (BHs) within GCs. Metal-poor GCs harbor a more massive and compact BH subsystem, which fosters more energetic few-body encounters, injecting greater kinetic energy into the stellar population. This extra energy, combined with the strong tidal forces in the galactic central regions, accelerates the dissolution of lower-metallicity GCs on timescales shorter than the host galaxy's age, leading to the emergence of a triangular depleted pattern in the R_g -[Fe/H] parameter space. Stronger tidal fields in more massive galaxies confine surviving metal-poor GCs to larger radii, broadening the depleted region. The depleted region's morphology may serve as a potential distance indicator for host galaxies. Our results also suggest that scenarios involving substantial BH natal kicks are unlikely, as too few retained BHs would erase the metallicity-dependent cluster dissolution required to form the observed depletion

Key words. Galaxies: structure – Galaxies: star clusters: general – globular clusters: general – Stars: black holes

2 Department of Physics, Faculty of Physics, Alzahra University,
3 Department of Physics, Institute for Advanced Studies in Basic Iran
4 Helmholtz-Institut für Strahlen-und Kernphysik (HISKP), University,
4 Helmholtz-Institut für Strahlen-und Kernphysik (HISKP), University,
8 Received XXX; accepted YYY

ABST

We analyzed the spatial distribution of globular cluster (GC) systed defined by projected galactocentric distances (Re) and metallicit characterized by a lack of metal-poor GCs in the inner parts of host be luminous mass of host galaxies; more massive galaxies consphenomenon to the combined influence of large-scale galactic ass of black holes (BHs) within GCs. Metal-poor GCs harbor a more few-body encounters, injecting greater kinetic energy into the steforces in the galactic central regions, accelerates the dissolution of age, leading to the emergence of a triangular depleted pattern in the galaxies confine surviving metal-poor GCs to larger radii, broade serve as a potential distance indicator for host galaxies. Our results unlikely, as too few retained BHs would erase the metallicity-dep region.

Key words. Galaxies: structure – Galaxies: star clusters: general

1. Introduction

The bimodal metallicity distribution of globular clusters (GCs) in most large host galaxies, such as the Milky Way (MW), implies the existence of two distinct subpopulations: metal-poor and metal-rich GCs (Zinn 1985; Forbes et al. 1997; Peng et al. 2006; Chies-Santos et al. 2012; Harris 2023; Hartman et al. 2023). These subpopulations exhibit dissimilarities in spatial distribution (Bassino et al. 2006; Peng et al. 2008; Strader et al. 2011; Pota et al. 2013), kinematics (Schuberth et al. 2013), and size (Kundu & Whitmore 1998; Jordán 2004; Harris 2009; Strader et al. 2011; Pota et al. 2013), kinematics (Schuberth et al. 2013), and size (Kundu & Whitmore 1998; Jordán 2004; Harris 2009; Strader et al. 2012; Pota et al. 2013), kinematics (Schuberth et al. 2010; the galaxy's stellar component, whereas the metal-poor GCs are though the galaxy's stellar component, whereas the metal-poor GCs are thought to be captured by the host galaxy through interactions with satellite galaxies (Forbes et al. 1997; Côté et al. 2000; Law & Majewski 2010; Tonini 2013; Pfeffer et al. 2018; Massari et al. 2019; Kruijssen et al. 2020; Rostami-Shirazi et al. 2022, 2024b).

Observational data from the MW GC system indicate that populations with different metallicities occupy distinct radial distributions. In particular, the inner part of the MW is almost depleted of metal-poor GCs (Harris 2001; Bica et al. 2006). The lack of metal-poor GCs at low mean Galactocentric distances (semi-major axes; a) follows a triangular pattern in the a-[Fe/H]

diagram (see Figure 1 in Rostami-Shirazi et al. 2024c, hereafter Paper I), indicating that GCs with lower metallicities appear further away from the Galactic center. Density analysis at a larger a, where both metal-poor and metal-rich GCs coexist, reveals that metal-rich GCs are significantly denser than their metal-poor counterparts (Paper I). This substantial density discrepancy implies that metal-poor GCs experience weaker gravitational binding, rendering them more vulnerable to tidal stripping and subsequent dissolution, suggesting a plausible explanation for their absence in the Galactic center. In Paper I, we interpreted the emergence of the triangular depleted region in the a-[Fe/H] diagram over Hubble time as a consequence of the increased vulnerability of metal-poor GCs to tidal destruction near the MW, coupled with the greater resilience of metal-rich GCs against dissolution. This pattern suggests a metallicity-dependent survival rate for GCs in the inner Galactic regions. Direct N-body simulations confirm that initial retention of black holes (BHs) in clusters leads to a significant disparity in evaporation rates between metal-poor and metal-rich clusters (Banerjee 2017; Chattopadhyay et al. 2022; Gieles & Gnedin 2023; Paper I).

Metallicity plays a crucial role in the evolution of massive stars, affecting the mass-loss rate through stellar winds and, consequently, the final mass of their remnants. Metal-poor clusters can host substantially more massive BHs than their metal-rich counterparts, as metal-rich progenitors undergo greater mass loss via stellar winds (Vink et al. 2001; Vink & de Koter 2005; Belczynski et al. 2008, 2010). Moreover, the range of masses

^{*} E-mail: ali.rostami.shirazi@ipm.ir

that convert to BHs is larger in metal-poor clusters (Shanahan & Gieles 2015). The heavier BH subsystem (BHSub) in metalpoor clusters, leads to stronger few-body encounters that inject increased kinetic energy into the entire stellar population. This results in greater expansion and higher evaporation rates compared to metal-rich clusters (Banerjee 2017; Chattopadhyay et al. 2022; Gieles & Gnedin 2023; Paper I). As a result, these clusters are more likely to dissolve within Hubble time, especially in the vicinity of the Galactic center, creating an empty triangular region in the a-[Fe/H] diagram. While metallicity-dependent BH dynamics can accelerate the disruption of low-metallicity clusters, it is likely only one of several mechanisms shaping the observed radial metallicity distribution of GCs. Large-scale processes such as hierarchical assembly, orbital decay, and tidal stripping in dense galactic environments likely act in concert with internal BH-driven heating.

Upon exhausting all thermonuclear energy sources, massive stars undergo gravitational collapse followed by supernova explosions, resulting in the formation of BHs as remnants (Oppenheimer & Snyder 1939; Iben & Renzini 1984; Heger et al. 2003). The mass and momentum ejected by the supernova are asymmetrically distributed, imparting a natal kick to the compact remnant. Constraining BH natal kicks relies on studying the kinematics of binary systems in the MW where a luminous companion is bound to a BH. However, results remain inconclusive: while some studies report evidence of substantial kicks, others find none (Atri et al. 2019; Zhao et al. 2023; Dashwood Brown et al. 2024; Vigna-Gómez et al. 2024; Nagarajan & El-Badry 2025). The debated magnitude of BH natal kicks creates uncertainties in the initial BH population retained in star clusters. Historically, BHs in GCs were considered unlikely due to the assumption that strong natal kicks could accelerate them beyond the GCs' escape velocity. However, since 2007, observations have confirmed the presence of BHs in GCs, suggesting that their natal kicks are weaker than previously thought (Maccarone et al. 2007; Shih et al. 2010; Barnard et al. 2011; Strader et al. 2012a; Chomiuk et al. 2013; Miller-Jones et al. 2015; Shishkovsky et al. 2018; Giesers et al. 2018, 2019; Saracino et al. 2022). Additionally, computational studies have shown that the retention of BHs is crucial to reproduce the observable properties of clusters accurately (Merritt et al. 2004; Mackey et al. 2007, 2008; Morscher et al. 2015; Peuten et al. 2016; Arca Sedda et al. 2018; Askar et al. 2018; Weatherford et al. 2018; Kremer et al. 2018; Askar et al. 2019; Kremer et al. 2019; Weatherford et al. 2020; Gieles et al. 2021; Torniamenti et al. 2023; Dickson et al. 2024; Paper I; Rostami-Shirazi et al. 2025a,b).

This paper focuses on the spatial distribution of GC systems within their host galaxies, specifically investigating whether the triangular region depleted of metal-poor GCs in the inner MW is a universal feature. Detecting this pattern across galaxies could provide additional evidence for the necessity of the initial BH retention within GCs. The paper is organized as follows: Section 2 outlines the impact of retained BHs on the spatial distribution of GCs, providing context for this study. The results are presented in Section 3, followed by a summary and conclusion in Section 4.

2. Impact of retained BHs on GC spatial distribution within host galaxies

The spatial metallicity distribution of GCs arises from the interplay of large-scale galactic processes and internal GC dynamics. In this context, the initial retention of BHs plays an essential role in driving the depletion of metal-poor GCs in the inner regions of

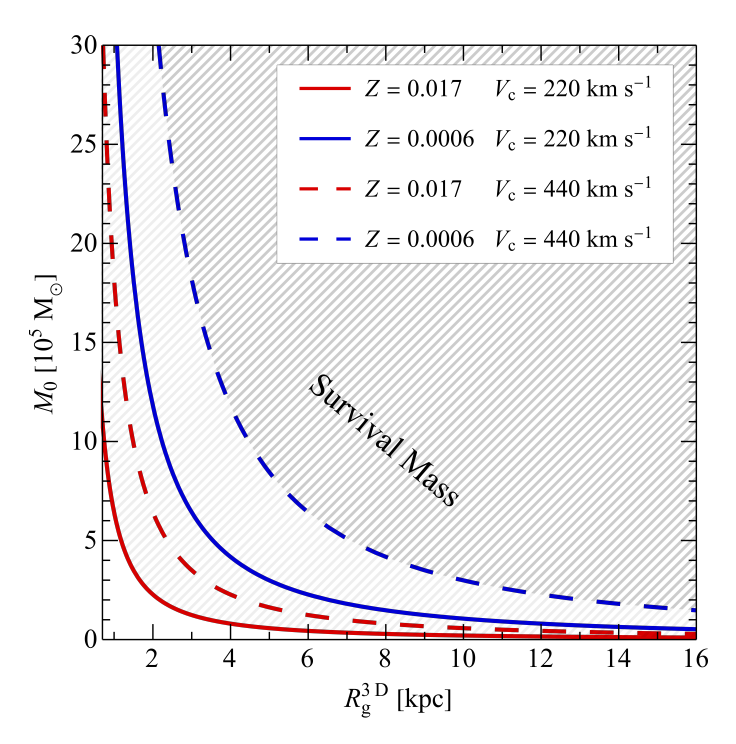


Fig. 1. Minimum prestellar evolution mass (M_0) required for GCs to survive over Hubble time $(\tau \ge 13.8\,\mathrm{Gyr})$, shown as a function of R_2^{3D} . Results are presented for Z=0.0006 (blue) and 0.017 (red) in host galaxies with circular velocities of $V_{\mathrm{c}}=220$ (solid lines) and $440\,\mathrm{km\,s^{-1}}$ (dashed lines). Each curve represents the survival mass threshold; GCs with M_0 above the corresponding curve (shaded region) remain bound over Hubble time.

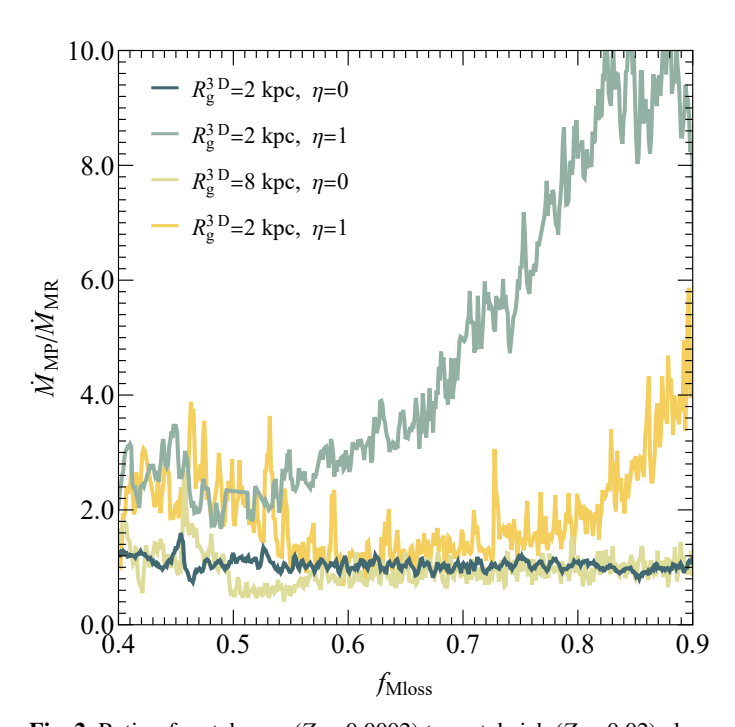


Fig. 2. Ratio of metal-poor (Z=0.0002) to metal-rich (Z=0.02) cluster mass-loss rates, $\dot{M}_{\rm MP}/\dot{M}_{\rm MR}$, as a function of the fractional mass loss, $f_{\rm Mloss}$. The modeled clusters follow the initial conditions of Paper I, except for a half-mass radius of $r_{\rm h,0}=1.2\,{\rm pc}$, and are located at $R_{\rm g}^{\rm 3D}=2$ and 8 kpc, covering BH retention from complete ejection ($\eta=0$) to full retention ($\eta=1$).

their host galaxies (see Section 3.5). In this section, we employ both literature-derived models (Section 2.1) and direct *N*-body simulations (Section 2.2) to examine how BH retention affects the metallicity-dependent dissolution of GCs and consequently the emergence of the depletion pattern.

The retention of a substantial BH population within the cluster after natal kicks triggers the formation of a BHSub at the cluster's center due to Spitzer instability (Spitzer 2014). This centrally segregated BHSub exhibits intense dynamical activity through subsequent encounters between BH-BH binaries and single BHs, injecting kinetic energy into the surrounding stellar population, which accelerates the cluster's evaporation rate (Heggie & Hut 2003; Breen & Heggie 2013; Banerjee 2017, 2018; Giesers et al. 2019; Wang 2020; Rostami-Shirazi et al. 2024a; Ghasemi et al. 2024). The mass fraction and average mass of BHs increase with decreasing metallicity (Vink et al. 2001; Vink & de Koter 2005; Belczynski et al. 2008, 2010; Shanahan & Gieles 2015). On the other hand, metal-rich clusters undergo enhanced stellar mass loss due to stronger stellar winds, which drives core expansion and results in longer core relaxation times (Vink & de Koter 2005; Schulman et al. 2012; Mapelli & Bressan 2013). The heavier and more rapidly relaxed BHSub in metal-poor clusters promotes more energetic few-body interactions, injecting more kinetic energy into the stellar population (Banerjee 2017; Chattopadhyay et al. 2022; Gieles & Gnedin 2023; Paper I).

In the inner galactic environment, the stronger tidal field limits the tidal radius, reducing the escape energy threshold for stars within clusters. This makes metal-poor GCs particularly susceptible to additional energy injection, which can propel stars beyond their escape velocity, dramatically accelerating their evaporation rate and potentially leading to dissolution within timescales shorter than the host galaxy's age. As galactic radius increases, clusters are subject to weaker tidal forces, resulting in higher escape velocities and a reduced influence of energy generated by the BHSub on the evaporation rates, thereby facilitating the survival of metal-poor GCs. Indeed, increased BHSub-driven heating in lower-metallicity clusters limits their long-term survival to larger three-dimensional galactocentric distances (R_g^{3D}). This process gives rise to a nearly void triangular pattern in the R_g^{3D} -[Fe/H] parameter space, characterized by a statistical depletion of metal-poor GCs. Stronger tidal forces in more massive galaxies would cause metal-poor GCs to survive only at greater $R_{\rm g}^{\rm 3D}$, thereby extending the triangular depleted region.

2.1. Literature-derived models

Gieles & Gnedin (2023), using direct *N*-body simulations, extended the mass-loss rate prescription of Baumgardt & Makino (2003) by incorporating the dynamical impact of BHs retained within GCs. Their models adopt the rapid supernova mechanism (Fryer et al. 2012), with fallback-dependent natal kicks, such that momentum conservation leads to the retention of 73% (50%) of the BH mass in metal-poor (metal-rich) clusters. They derived a generalized mass-loss rate expressed as

$$\dot{M} = \dot{M}_{\text{ref}} \left(\frac{M}{M_{\text{i}}} \right)^{1-y} \left(\frac{M_{\text{i}}}{2 \times 10^5 \, M_{\odot}} \right)^{1/3} \left(\frac{\Omega_{\text{tid}}}{0.32 \, \text{Myr}^{-1}} \right), \tag{1}$$

where $M_{\rm i}$ is the post-stellar-evolution initial mass, $\Omega_{\rm tid}$ quantifies the strength of the external tidal field, y and $\dot{M}_{\rm ref}$ are free parameters calibrated through N-body simulations. Notably, for an initial density within the half-mass radius of $\rho_{\rm h,0}=300\,{\rm M}_{\odot}~{\rm pc}^{-3}$ in

metal-rich clusters (Z=0.017 and 0.006), the best-fitting parameters are $M_{\rm ref}=-30\,{\rm M}_\odot$ Myr $^{-1}$ and y=2/3, corresponding to a gradual "skiing" mass-loss regime. In contrast, for metal-poor clusters (Z=0.0006), the higher BH retention fraction leads to $M_{\rm ref}=-45\,{\rm M}_\odot$ Myr $^{-1}$ and y=4/3, indicative of an accelerated "jumping" disruption mode. Their models assume a fixed initial filling factor, defined as the ratio of the half-mass radius to the effective Jacobi radius, $r_{\rm h,0}/r_{\rm J,eff}\simeq 0.05$. Although this value is a simplification and real clusters exhibit a range of filling factors and orbital conditions, it serves as a reasonable approximation to the average structural properties of surviving MW GCs.

Figure 1 illustrates how the metallicity-dependent massloss trends map onto cluster survival by showing the minimum prestellar evolution mass, M_0 , taken as $2 \times M_i$ under the assumption of $\sim 50\%$ stellar evolutionary mass loss. This is the mass required for a GC to survive the Hubble time at a given $R_{\rm g}^{\rm 3D}$, derived via time integration of Equation 1, across different metallicities and host-galaxy tidal field strengths. At each metallicity, the curves delineate the survival mass boundary: clusters above the curve (shaded region) remain long-lived, while those below dissolve within Hubble time. The boundary is strongly metallicity- and tide-dependent, particularly in the inner regions of the host galaxies. Lower–metallicity systems demand larger $R_{\rm g}^{\rm 3D}$ (or higher M_0) to survive, with the shift amplified in more massive galaxies (i.e., those with larger circular velocities $V_{\rm c}$).

As an illustrative case, GCs born with $M_0 \simeq 2 \times 10^5 \, \mathrm{M_\odot}$ require $R_{\rm g}^{\rm 3D} \gtrsim 6.5 \, \mathrm{kpc}$ to survive in a $V_{\rm c} = 220 \, \mathrm{km \, s^{-1}}$ field, whereas their metal-rich counterparts can persist at radii as small as 2 kpc. In a stronger tidal field ($V_{\rm c} = 440 \, \mathrm{km \, s^{-1}}$), the corresponding thresholds shift outward to $\gtrsim 13 \, \mathrm{kpc}$ and $\gtrsim 4 \, \mathrm{kpc}$, respectively. A complementary perspective is provided at fixed $R_{\rm g}^{\rm 3D} = 4 \, \mathrm{kpc}$ in the $V_{\rm c} = 440 \, \mathrm{km \, s^{-1}}$ model: clusters with Z = 0.0006 require $M_0 \gtrsim 1.15 \times 10^6 \, \mathrm{M_\odot}$ to survive, nearly an order of magnitude higher than the $M_0 \gtrsim 2.1 \times 10^5 \, \mathrm{M_\odot}$ needed for Z = 0.017 or 0.006. At larger $R_{\rm g}^{\rm 3D}$, these offsets diminish as the survival thresholds converge. This pronounced disparity in survival mass at small $R_{\rm g}^{\rm 3D}$ reveals that metal-rich clusters are far less susceptible to disruption in the inner galaxy, whereas metal-poor GCs face significantly stricter survival constraints, leading to a statistical depletion in the $R_{\rm g}^{\rm 3D}$ –[Fe/H] parameter space.

2.2. N-body simulations

In Paper I, we conducted two sets of *N*-body simulations for both metal-poor and metal-rich models, varying the BH natal kick velocities between low and high. Under the assumption that all BHs are promptly ejected following their formation, we found that the dissolution times of metal-poor and metal-rich clusters were nearly identical, with no evidence for a depleted population of metal-poor clusters in the inner regions of the host galaxy. In contrast, our results indicated that the dissolution time—metallicity correlation is contingent upon the initial retention of BHs within the modeled clusters.

The evolution and eventual self-depletion of the BHSub are governed by the flow of energy through the cluster's half-mass radius, which is primarily regulated by its two-body relaxation time (Breen & Heggie 2013). In initially compact clusters, short relaxation times drive rapid energy transfer from the BHSub to the stellar component and hence prompt BHSub depletion; by contrast, tidally filling or moderately under-filling systems can expand more effectively, lengthening the relaxation time and prolonging BHSub longevity. Following Paper I, we performed an additional suite of *N*-body simulations with a more compact

initial configuration, better representing the densities inferred for MW GCs. All models have an initial mass of $M_0 = 6 \times 10^4 \, \mathrm{M}_\odot$. The initial half-mass radius was set to $r_{\mathrm{h},0} = 1.2 \, \mathrm{pc}$, based on the Marks & Kroupa (2012) relation after gas expulsion, assuming an expansion factor of three (Baumgardt & Kroupa 2007). We explore two bracketing metallicities, Z = 0.0002 and Z = 0.02, and two limiting prescriptions for BH retention, $\eta \in \{0,1\}$, corresponding to the complete ejection ($\eta = 0$) and the full retention of the nascent BH population ($\eta = 1$). Figure 2 presents the ratio of mass-loss rates of metal-poor to metal-rich models, $\dot{M}_{\mathrm{MP}}/\dot{M}_{\mathrm{MR}}$, at $R_{\mathrm{g}}^{\mathrm{3D}} = 2$ and 8 kpc, shown as a function of the mass-loss fraction f_{Mloss} .

In the $\eta = 0$ case, metal-poor and metal-rich clusters lose mass at nearly identical rates throughout their evolution, $\dot{M}_{\rm MP}/\dot{M}_{\rm MR} \approx 1$. By contrast, in the $\eta=1$ case, the ratio becomes strongly radius-dependent: at $R_{\rm g}^{\rm 3D}=2$ kpc it rises steeply, reaching up to $\dot{M}_{\rm MP}/\dot{M}_{\rm MR}=10$, while at 8 kpc the excess persists but is more modest. This behavior reflects the interplay between (i) stronger dynamical heating from the heavier BHSub in metal-poor clusters and (ii) the external tide. Near the galaxy center, the reduced Jacobi radius lowers the escape energy, so BH-driven heating is efficiently converted into escapees and an elevated $M_{\rm MP}$; farther out, the same heating has a diminished effect because the tidal boundary is wider, and, simultaneously, fractional BH mass gradually decreases due to self-depletion, reducing its contribution to the mass-loss rate. At still larger radii, the ratio asymptotes to unity, and metal-poor and metalrich clusters evolve similar to BH-free systems after their BH-Subs are exhausted.

Crucially, even for these compact initial conditions, metalpoor clusters at small R_g^{3D} experience significantly stronger dynamical heating, shortening their survival times below Hubble time. This effect is further amplified in more massive galaxies, where stronger tidal fields reduce the Jacobi radius and increase the cluster's tidal filling. Adopting fallback-dependent natal kicks instead of the $\eta = 1$ idealization would increase the metallicity contrast in initial BH fractions. The most massive BHs, formed via the direct stellar collapse, are subject to minimal kicks. Since high-mass BHs are more populated in metalpoor clusters, their retention fraction would be higher, leading to a further amplification of the mass-loss rate ratio $\dot{M}_{\rm MP}/\dot{M}_{\rm MR}$ shown in Figure 2. Observational hints of top-heavy initial mass functions (Marks et al. 2012) in low-metallicity environments would further exacerbate $\dot{M}_{\rm MP}/\dot{M}_{\rm MR}$ by seeding even more massive BHSubs, making dissolution likely even in initially tidally under-filling systems (Chatterjee et al. 2017; Giersz et al. 2019).

2.3. Caveats

Gieles & Gnedin (2023) simulated clusters that correspond to the low-*N*, low-density regime of GC evolution, where the impact of BH-driven dynamical heating on mass loss is enhanced. However, more massive and denser GCs often remain in an expansion-dominated phase over Hubble time, where the relaxation timescale, rather than BH heating, primarily regulates the mass-loss rate. Consequently, extrapolation of Equation 1 to higher-*N*, higher-density clusters should be approached with caution, as the resulting metallicity dependence of the mass-loss rate may be weaker than inferred from the lower-density models.

Although our simulations roughly reproduce the initial densities of MW GCs, our models have lower *N* than typical MW GCs. This limitation arises from current computational constraints: fully resolved *N*-body simulations with realistic stellar

numbers, binary fractions, and remnant populations remain extremely demanding. The extent of the depleted region in $R_{\rm g}^{\rm 3D}$ -[Fe/H] space is sensitive to the initial N: clusters with more typical N would dissolve more slowly, since GC dissolution times scale approximately with the half-mass relaxation time. Consequently, the resulting depletion region would be smaller, implying that the relative contribution of BH dynamics to the depletion of inner-galaxy metal-poor GCs may be reduced compared to large-scale galactic processes such as hierarchical assembly. Future studies employing higher-N models and dense initial configurations will be essential to quantitatively assess the strength of metallicity-dependent BH dynamics in shaping GC survival across diverse galactic environments.

3. Results

To investigate the spatial distribution of GC systems, we analyzed a sample of 37 host galaxies, encompassing both early-type and late-type galaxies. The results of this analysis are discussed in the following sections.

3.1. The $R_{\rm g}$ -[Fe/H] distribution of GC systems in host galaxies

We constructed a two-dimensional parameter space using projected galactocentric distances $(R_{\rm g})$ and metallicity ([Fe/H]), where each GC occupies a point within this space. The list of galaxies, along with the associated references for their GC system data $(R_{\rm g}$ and [Fe/H]), is compiled in Table A.1. We utilize the multivariate (two-dimensional) probability density function (PDF) and cumulative distribution function (CDF) of GCs in the aforementioned parameter space as criteria to determine the spatial distribution patterns of metal-poor and metal-rich GCs in their host galaxies.

We employ Gaussian kernel density estimation (KDE) through the scikit-learn library in Python, specifically utilizing the KernelDensity estimator to derive both the PDF and CDF, with an automatic bandwidth selection method to optimize smoothing. The Gaussian kernel provides a smooth estimate of the underlying distribution, effectively capturing its structure. To visualize the distribution, we calculate isodensity contours based on the derived PDF and CDF. These contours are drawn at specific quantiles, representing boundaries that enclose certain percentages of the data. By analyzing these contours, we can identify regions where GCs are least likely to be found.

Figure 3 illustrates the CDF and scaled PDF for eight galaxies, along with their corresponding isodensity contours. The PDFs for NGC 3258, NGC 1132, NGC 1272, UGC 9799, and NGC 4874 exhibit two distinct peaks: one associated with low metallicity and the other with high metallicity, reflecting the known bimodal metallicity distribution of GCs. As we move away from the peaks, the PDF asymptotically approaches zero, indicating regions where the probability of finding GCs is extremely low. Figure 3 clearly demonstrates that the probability of locating the metal-poor population in the inner parts of the host galaxies is very low, with a specific trend: as the metallicity of GCs decreases, there is a corresponding reduction in the probability of their presence at smaller $R_{\rm g}$. This pattern was consistently observed in the PDFs of all 37 galaxies examined in this study.

This result mirrors the triangular depleted region observed in the mean Galactocentric distances, a, versus [Fe/H] diagram for the MW GC population, as discussed in Paper I. It is noteworthy that using $R_{\rm g}^{\rm 3D}$ or mean galactocentric distances, rather

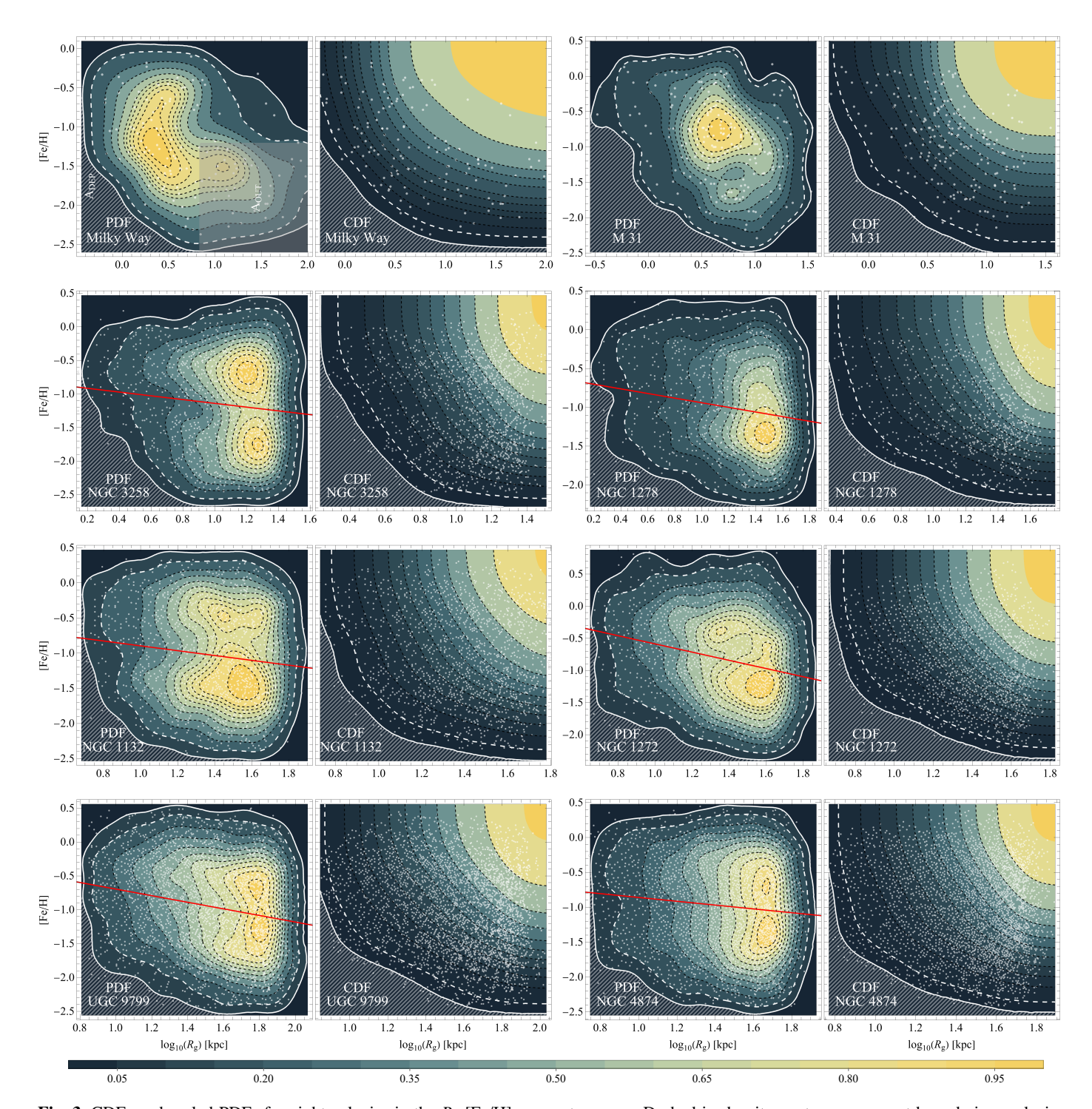


Fig. 3. CDFs and scaled PDFs for eight galaxies in the R_g -[Fe/H] parameter space. Dashed isodensity contours represent boundaries enclosing 5-95% of all data in 10% increments. White contours (dashed for 95% and solid for 99%, respectively) mark outer boundaries. Gray dots denote the distribution of GCs in each host galaxy. The hatched area highlights the depleted region of metal-poor GCs ($A_{\rm DEP}$), while the shaded area in the MW panel indicates the outer non-depleted region ($A_{\rm OUT}$; see Section 3.2). Red solid lines show the least-squares fitted metallicity gradient (Harris 2023; see Section 3.5). The CDFs are derived from the clustering results of the DBSCAN algorithm, with low-density regions excluded and classified as noise.

than $R_{\rm g}$, would amplify the observed depletion pattern of metal-poor GCs. However, the lack of three-dimensional data for most galaxies constrained this analysis. Projection effects may account for the apparent presence of metal-poor GCs in the inner regions of galaxies. Utilizing three-dimensional distances would push these clusters outward in parameter space, making the depleted region more distinct.

The CDF provides further insights into the spatial distribution of GCs. To construct the CDF, we applied the Density-Based Spatial Clustering of Applications with Noise (DBSCAN) algorithm through the scikit-learn library in Python, an effective unsupervised machine-learning technique that identifies clusters based on density variations (see, e.g., Castro-Ginard et al. 2018). DBSCAN excels at distinguishing dense core re-

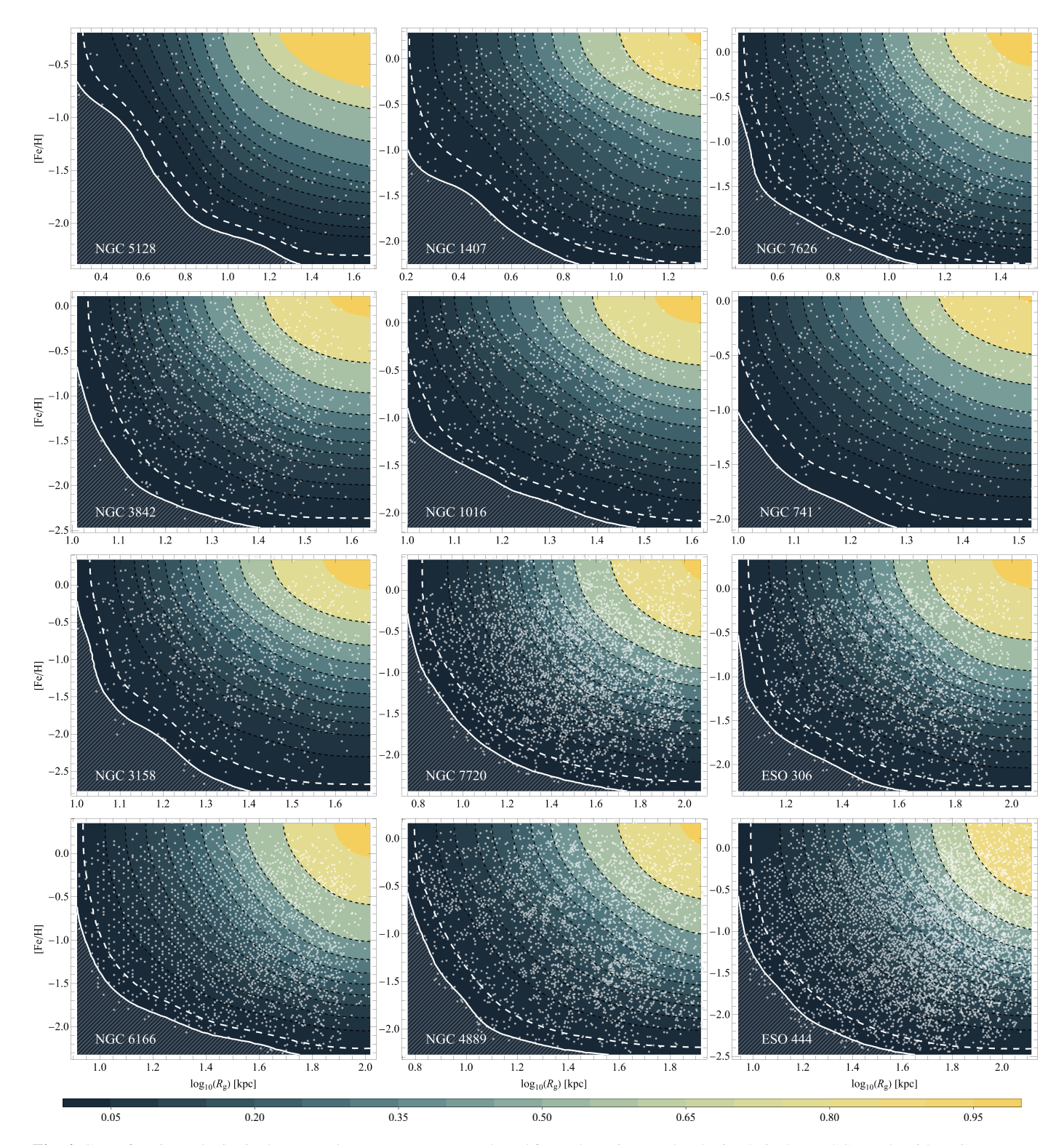


Fig. 4. CDFs for nine galaxies in the R_g -[Fe/H] parameter space, plotted from clustering results obtained via the DBSCAN algorithm. Contours are plotted similarly to those in Figure 3. The white contours mark boundaries that encompass 95 and 99% of the data, highlighting regions with very low probabilities of finding GCs, corresponding to approximate CDF values of 0.01 and 0.002. The hatched area highlights the depleted region of metal-poor GCs.

gions from sparse, low-probability points labeled as noise; in our implementation, the neighborhood radius (ϵ) was defined as the average width of a grid cell in a uniform 10×10 partitioning of the parameter space. We set the minimum number of points required to form a cluster to $\sim 1\%$ of the total dataset, excluding

low-density regions below this threshold as noise. By systematically filtering out these areas, DBSCAN makes the depleted region of host galaxies more pronounced, while also mitigating the projection effects that could obscure the intrinsic spatial structure of GCs. The CDFs presented in Figure 3 further highlight

the marked scarcity of metal-poor GCs in the inner regions of these galaxies, following a distinct triangular pattern.

Figure 4 shows the CDF for nine additional galaxies, highlighting the sparse distribution of metal-poor GCs in the inner regions across all galaxies. The solid white contours, which encompass 99% of the data (corresponding to approximate CDF values of 0.002), outline large inner areas with a low probability of finding metal-poor GCs.

3.2. Statistical tests

To systematically assess the sparsity of metal-poor GCs in the inner regions of host galaxies, we now apply a series of statistical tests. These methods allow us to quantify the significance of the depleted region and determine whether the observed patterns are statistically robust rather than a random fluctuation.

3.2.1. Total probability ratio

As a first step in our statistical analysis, we introduce a probability ratio metric that compares the observed probability of metalpoor GCs within the depleted region to their expected probability under the assumption that they follow the spatial distribution of metal-rich GCs. The depleted region (A_{DEP}) is defined as the area outside the contour enclosing 99% of the data in the PDF, situated in the inner regions of the host galaxy (indicated by the hatched area in the PDFs of Figure 3). The total probability of finding a metal-poor GC in the depleted region, as derived from the observed PDF, is denoted as P_{DEP}. To estimate the expected probability, we assume that metal-poor GCs follow the same spatial distribution as metal-rich ones. To model this scenario, we construct a flipped probability density function (PDF_{flip}), which mirrors the distribution of metal-rich GCs. We then compute the total probability based on PDF_{flip} in A_{DEP} , denoted as $P_{flip,DEP}$. Finally, we define the total probability ratio as

$$\tilde{P}_{DEP} = \frac{P_{flip,DEP}}{P_{DEP}}.$$
(2)

For comparison, we repeat the same procedure for the non-depleted region (A_{OUT}), defined as the rectangular area beyond the outer edge of the A_{DEP} , extending from the maximum depletion radius and restricted to GCs with [Fe/H] < -1.2 (shown as the shaded area in the MW panel of Figure 3). The corresponding probability ratio is denoted as $\stackrel{\sim}{P}_{OUT}$.

The results, presented in Table A.1, show that P_{DEP} is consistently much larger than 1 across all galaxies, with an average value of 7.69. This suggests that if metal-poor GCs in the inner regions followed the same distribution as metal-rich ones, their probability density would be approximately eight times higher than what is observed. In contrast, the values of \tilde{P}_{OUT} are close to 1 for most galaxies, with an average of 1.36, indicating that outside the depleted region, the probability density of metal-poor and metal-rich GCs is nearly identical. These results provide statistical evidence that the inner regions of host galaxies are indeed areas of anomalously low probability for metal-poor GCs. The probability density of metal-poor GCs within these regions differs significantly from that of their metal-rich counterparts, reinforcing the conclusion that metal-poor GCs are preferentially rare in the inner galactic regions.

3.2.2. Nearest neighbor distance ratio

While the total probability ratio provides a global measure of sparsity, a more localized approach can offer further insights. To this end, we examine the nearest neighbor distances of GCs within the depleted region, providing a direct measure of clustering. This allows us to compare the local probability density of metal-poor GCs with the expected distribution if they followed the spatial pattern of metal-rich GCs. We first compute the mean nearest neighbor distance for metal-poor GCs inside the depleted region. To establish a reference distribution, we assume that metal-poor GCs follow the same spatial pattern as metalrich ones and compute the corresponding mean nearest neighbor distance using the flipped probability density function, PDF_{flip}. The ratio of these reference and observed values is denoted as NND_{DEP}. A value significantly smaller than 1 indicates that metal-poor GCs in the depleted region are much more sparsely distributed than metal-rich GCs. We repeat the same calculation for A_{OUT}, defining the corresponding ratio as NND_{OUT}.

The results, summarized in Table A.1, reveal a significant difference in clustering behavior between the depleted and nondepleted regions. In the depleted region, NND_{DEP} is consistently much smaller than 1 across all galaxies, with an average value of 0.33; for several galaxies, this value is zero, indicating that the depleted region is either completely devoid of metal-poor clusters or contains only one cluster, which leads to an infinite nearest neighbor distance. This indicates that the typical nearest neighbor distance for metal-poor GCs in the depleted region is approximately three times larger than expected under a metalrich-similar distribution, reinforcing the conclusion that metalpoor GCs are much more sparsely distributed in the central regions of galaxies. In contrast, NND_{OUT} is close to 1 for most galaxies, with an average of 0.93, suggesting that outside the depleted region, the clustering properties of metal-poor and metalrich GCs are nearly identical.

3.2.3. Chi-square test

To further test whether the observed spatial depletion of metalpoor GCs is statistically significant, we apply a chi-square test. This allows us to compare the observed GC distribution with expectations derived from the assumed spatial pattern of metalrich GCs. The phase space was divided into a 10×10 grid, partitioning both R_g and [Fe/H] into ten equal bins. Within A_{DEP} , we compared the observed and expected distributions of GCs, where the expected values were derived from PDF_{flip}. The goodness of fit between the observed and expected distributions was assessed using a chi-square (χ^2) test, with the corresponding pvalue (p_{χ^2}) , which quantifies the statistical significance of the deviation. The null hypothesis states that the observed distribution of metal-poor GCs in the depleted region follows the same spatial pattern as metal-rich GCs. A small p_{χ^2} indicates that the null hypothesis should be rejected, indicating that the observed distribution significantly deviates from the expected one.

The results detailed in Table A.1 show that for most galaxies, p_{χ^2} falls below the conventional threshold of 0.05, indicating a significant deviation between the observed and expected distributions. These results provide further statistical confirmation that metal-poor GCs in the inner regions exhibit a markedly different spatial distribution compared to metal-rich GCs. The average p_{χ^2} across all studied galaxies is 0.07, reinforcing the conclusion that the scarcity of metal-poor GCs in the inner re-

gions is unlikely to be a random fluctuation. Instead, a physical effect is responsible for this depletion.

3.2.4. Poisson distribution analysis

In addition to the chi-square test, we use a Poisson distribution analysis to evaluate whether the observed number of metal-poor GCs in the depleted region is consistent with expectations. This provides an independent statistical check on the robustness of our findings. Using the total probability values obtained in Section 3.2.1, we compute the expected and observed cluster counts by multiplying the total probability by the total number of GCs in each galaxy. The Poisson probability, p_{Poisson} , quantifies the likelihood of obtaining the observed count given the expected value.

The results in Table A.1 indicate that $p_{Poisson}$ approaches zero for nearly all galaxies. This suggests that the observed number of metal-poor GCs in the depleted region is highly improbable if they follow the spatial pattern of metal-rich GCs. The low probability values reinforce the conclusion that the scarcity of metal-poor GCs in the inner regions is not a statistical fluctuation but a physical effect. It is important to note that the validity of the Poisson approach depends on sample size, as the distribution becomes less meaningful for large expected counts. However, since the number of metal-poor GCs in the depleted region is relatively small across all galaxies, the Poisson model remains appropriate.

3.2.5. Kolmogorov-smirnov test

Finally, we perform a Kolmogorov-Smirnov (K-S) test to compare the metallicity distributions of metal-poor and metal-rich GCs. This test helps to determine whether the two populations originate from the same parent distribution, providing further information on the significance of the depleted region. Since the K-S test is inherently one-dimensional, we used only the metallicity values of GCs for this analysis. The inner surface was defined by first determining the largest radius within which the depleted region pattern exists. We then considered all clusters with [Fe/H] < -1.2 within this radius. The observed and expected metallicity distributions were then obtained as before, with the expected distribution derived from PDF_{flip}. We computed the K-S test statistic and corresponding p-value for this region, $p_{\text{KS-DEP}}$. The same procedure was applied to the outer region, corresponding to A_{OUT} , yielding $p_{\text{KS-OUT}}$.

The results reveal a striking contrast between the inner and outer regions (Table A.1). For many galaxies, $p_{\rm KS-DEP}$ is below the conventional 0.05 threshold, with an average value of 0.03, indicating that the distributions of metal-poor and metal-rich GCs in the inner regions are statistically distinct. This strongly suggests that the presence of the depleted region plays a key role in differentiating the two populations. In contrast, $p_{\rm KS-OUT}$ is greater than 0.05 for most galaxies, with an average value of 0.36. This implies that outside the depleted region, the distributions of metal-poor and metal-rich GCs are much more similar, and there is no strong statistical evidence to reject the hypothesis that they originate from the same parent distribution.

These findings reinforce the conclusion that the depletion of metal-poor GCs in the inner regions is not a random fluctuation but a real effect that significantly alters the distribution. The stark contrast between $p_{\rm KS-DEP}$ and $p_{\rm KS-OUT}$ further confirms that the primary factor distinguishing metal-poor and metal-rich GCs in the inner galaxy is the presence of the depleted region, whereas in the outer galaxy, their distributions are more comparable.

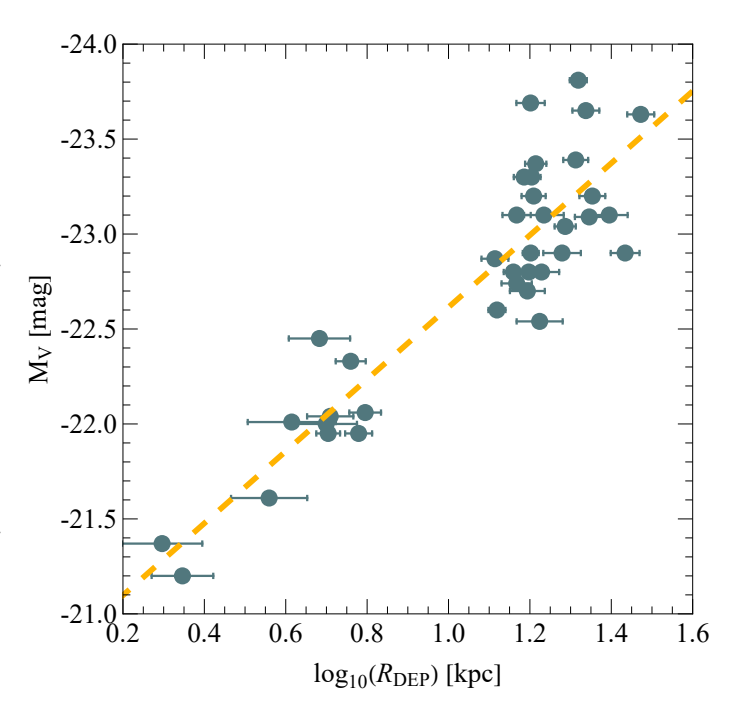


Fig. 5. Mean $R_{\rm DEP}$ versus V-band absolute magnitude of host galaxies (M_V) . Error bars indicate the standard deviation of $R_{\rm DEP}$. The fitted dashed line reveals the trend that more luminous galaxies tend to have larger $R_{\rm DEP}$ values, with a Pearson correlation coefficient of 0.9.

The influence of host galaxy luminosity on depletion morphology

To quantify the influence of the host galaxy's tidal field on the morphology of the depleted region, we define the depopulation radius, $R_{\rm DEP}$, in the $R_{\rm g}$ -[Fe/H] diagram. This parameter is defined as the distance at which the probability of encountering a cluster with [Fe/H] = -2.0 surpasses 1% in the host galaxies. In other words, $R_{\rm DEP}$ is the distance at which the CDF for GCs with [Fe/H] = -2.0 reaches 0.01. Mathematically, this can be expressed as

$$f_{\text{CDF}}(R_{\text{DEP}}, [\text{Fe/H}] = -2.0) = 0.01,$$
 (3)

where f_{CDF} represents the CDF of the GC distribution in the host galaxy. R_{DEP} serves as a proxy for the boundary beyond which metal-poor GCs ($[Fe/H] \ge -2.0$) can persist against tidal disruption. We assume that this metric represents the edge of the depleted region. The integrated V-band absolute magnitude (M_V ; see Table A.1) versus R_{DEP} for the complete set of 37 galaxies in our study is visualized in Figure 5. We used bootstrap resampling to determine R_{DEP} for each galaxy, generating 1000 iterations of galaxy's CDF while preserving the original GC count. $R_{\rm DEP}$ was calculated for each iteration, and the average values, with standard deviation as error bars, are shown in Figure 5. This method accounts for statistical uncertainties in $R_{\rm DEP}$. Figure 5 shows a strong positive correlation between R_{DEP} and M_V , with a Pearson correlation coefficient of 0.9, suggesting that metalpoor GCs survive farther from more luminous galaxies, thereby shifting the survival boundary to larger R_g . Although $R_{\rm DEP}$ is defined using [Fe/H] = -2.0 and $f_{CDF} = 0.01$, similar trends appear for other metallicities and thresholds.

Our initial hypothesis proposed a link between the morphology of the depleted region of metal-poor GCs and the total mass of their host galaxies. However, our results reveal a direct correlation with luminous mass. This result aligns with interpreta-

tions based on modified gravity theories or the Λ CDM framework. Interestingly, the correlation between $R_{\rm DEP}$ and M_V indicates that the morphology of the metal-poor GC depleted region has potential as a novel distance indicator, offering an alternative method for measuring galactic distances. Figure 5 showcases a heterogeneous sample of galaxies, encompassing Brightest Cluster Galaxies (BCGs) and ordinary field galaxies. Despite the distinct formation histories of these galaxy types, we did not separate them in this analysis. To develop a reliable method for galactic distance measurement, future studies may need to categorize galaxies based on their types and analyze them separately (Rostami-Shirazi et al., in prep.).

3.4. Robustness of $R_{\rm DEP}$ calculations among limited central GC data in galaxies

Studying GC systems presents a notable challenge, as data for many galaxies is typically available only from a few kpc outward. This limitation arises from the difficulty of detecting GCs against the bright background of the galaxy center, where the light often obscures their measurement. Consequently, detailed central GC distributions are generally restricted to the MW, M31, and a few Local Group galaxies. While this constraint could affect R_{DEP} calculations, our methodology demonstrates resilience. For instance, in the case of UGC 10143, where GC data is available for $R_g > 3$ kpc, we compared the CDF contours at 0.01 and 0.002 levels using the full dataset and a subset excluding data within 10 kpc. As shown in Figure 6, the contours converged at low metallicities, with R_{DEP} calculations differing by less than 1% between the two datasets. Repeating this test for other galaxies consistently showed errors below a few percent, confirming that our method effectively accounts for the lack of central GC distribution data. Indeed, the pattern of depleted regions extends several kpc from the galaxy center. Even in the absence of GC distribution data in the central regions, the calculation of R_{DEP} remains robust.

The mass and characteristic radius of stellar systems (including galaxies) typically correlate with each other. It is therefore natural to expect that this mass-radius correlation would also apply to the total mass and radial extent of any early central star formation episode. Consequently, in more massive galaxies, the region where metal-rich central clusters are formed is expected to be more extended. While this provides a structural expectation, additional dynamical effects influence the survival and spatial distribution of clusters in these inner regions, depending on the mass of the host galaxy. However, our analysis may not fully capture the complex dynamics of inner galactic regions, where additional external effects such as rapidly varying tidal forces (Gnedin & Ostriker 1997), tidal shocks from disk crossings (Gnedin et al. 1999), interactions with giant molecular clouds (Gieles et al. 2006), and spiral arm influences (Gieles et al. 2007) can significantly contribute to GC dissolution. This caveat underscores the need for further investigation into these factors when interpreting our results for the inner galactic regions.

3.5. Depleted regions and galactic assembly histories

The assembly scenario for GC system formation posits that metal-poor GCs are primarily captured from satellite galaxies, resulting in a broader spatial distribution than that of metal-rich GCs. In addition, major mergers involving gas-rich progenitors can trigger the formation of new, centrally concentrated

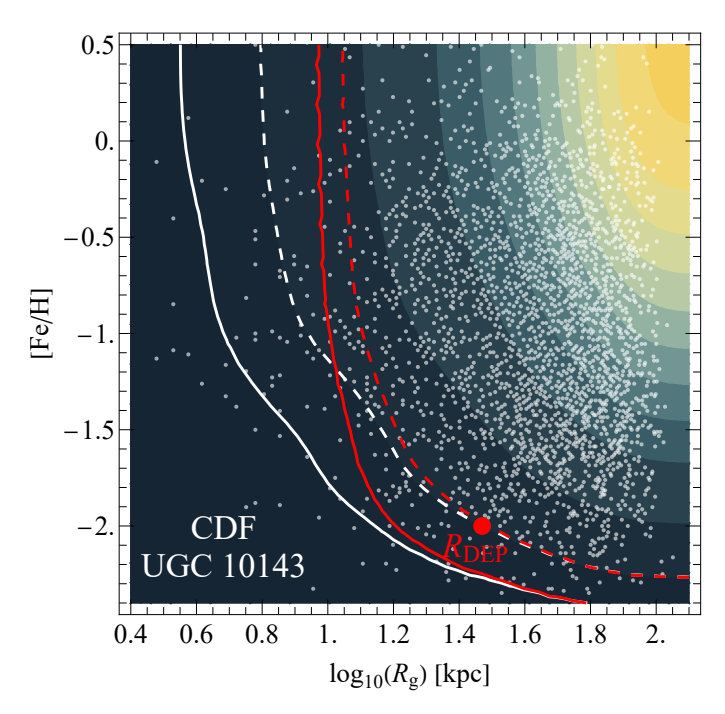


Fig. 6. CDF for the galaxy UGC 10143 in the $R_{\rm g}$ -[Fe/H] parameter space. White contours show the CDF for the full dataset (dashed line: $f_{\rm CDF} = 0.01$; solid line: $f_{\rm CDF} = 0.002$). Red contours represent the CDF calculated using only data with $R_{\rm g} > 10\,{\rm kpc}$ (same line style convention). The red dot marks the location of $R_{\rm DEP}$.

metal-rich clusters, while simultaneously redistributing preexisting metal-poor GCs to larger radii through angular momentum transfer (Bekki et al. 2002; Li et al. 2004). These mechanisms successfully account for the observed metallicity gradients with $R_{\rm g}$, where the average metallicity of GCs decreases as $R_{\rm g}$ increases. Red solid lines in Figure 3 illustrate this trend, showing least-squares fits in the form

$$[Fe/H] = a + b \log_{10}(R_g).$$
 (4)

Harris (2023) demonstrated shallow gradients in mean metallicity for most galaxies in their sample, with a mean power-law exponent of $\langle b \rangle = -0.3$ across the entire dataset and, notably, no clear trend with galaxy luminosity. While the shallow metallicity gradient is well justified by both assembly and major merger scenarios, it appears insufficient to fully explain the observed triangular depleted region of metal-poor GCs in the inner parts of galaxies. Crucially, we observed a clear correlation between the morphology of this depleted region and the luminous mass of galaxies, a trend not present in the metallicity gradients.

To assess whether the observed depleted region is solely a signature of the assembly history, we constructed PDFs of the MW GC system, separating insitu formed clusters from exsitu accreted ones. A common approach for this classification is to distinguish GCs in the space of Galactic orbital energy and out-of-plane angular momentum, often associating them with known interacting events (e.g., Massari et al. 2019; Naidu et al. 2020; Malhan et al. 2022; Bonaca & Price-Whelan 2025). Figure 7 shows the PDF of the MW GCs restricted to the insitu population, based on three independent classification schemes. Massari et al. (2019) associate ~ 35% of MW GCs with major mergers, including Gaia-Enceladus, the Sagittarius dwarf galaxy, the Helmi streams, and the Sequoia galaxy. Malhan et al. (2022) employed a clustering algorithm in action space to identify six

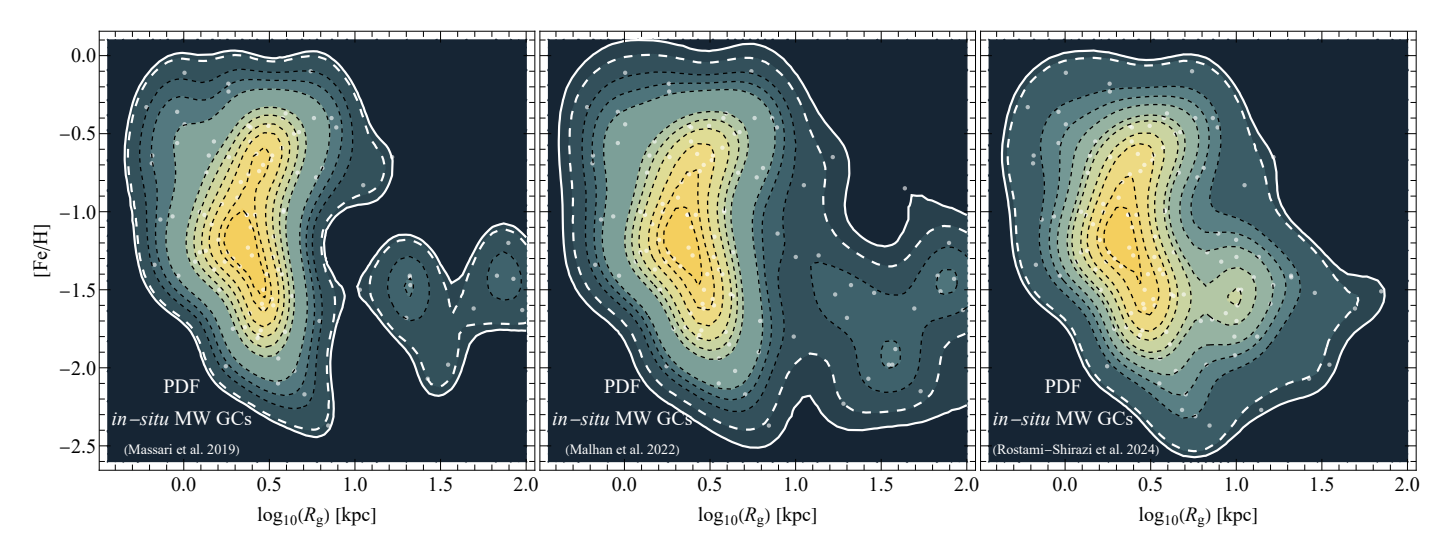


Fig. 7. Scaled PDFs of MW GCs restricted to the insitu population, analogous to Figure 3. Exsitu GCs are excluded based on Massari et al. (2019; left panel), Malhan et al. (2022; middle panel), and Rostami-Shirazi et al. (2024b; right panel).

distinct merger events, including Pontus. Rostami-Shirazi et al. (2024b) performed kinematic simulations to trace potential GC capture from 41 dwarf satellite galaxies, identifying 29 likely exsitu candidates. The PDFs derived from all three studies consistently reveal that, even when exsitu clusters are excluded, the triangular depleted region of metal-poor GCs remains clearly evident. Quantitatively, the value of $R_{\rm DEP}$ changes by less than 6% compared to the analysis of the full GC sample. This suggests that the depleted region is not merely a byproduct of the Galaxy's hierarchical assembly.

Although hierarchical assembly naturally predicts a broader spatial distribution for metal-poor GCs, it falls short of reproducing the distinct triangular morphology of the depleted region and its systematic dependence on galaxy luminosity. These features instead point toward an additional, internally driven mechanism operating within the GCs themselves. BH dynamics provides a plausible contributing factor to both the universality of the depletion pattern and its scaling with host galaxy mass. This mechanism likely acts in concert with large-scale processes, such as hierarchical accretion histories and environmental effects, in shaping the spatial metallicity distribution of GCs. A quantitative validation of this interpretation remains essential. Specifically, determining the slope of the $R_{\rm DEP}-M_V$ trend from simulations and comparing it with the observed trend (Figure 5) constitutes a key test, which will be the focus of a future study.

4. Summary and conclusion

We analyzed the spatial distribution of GC systems in 37 host galaxies by examining their PDFs and CDFs in the $R_{\rm g}$ -[Fe/H] parameter space. Our investigation revealed a universal triangular depleted region, marked by a distinct lack of metal-poor GCs in the inner parts of galaxies. This pattern demonstrates that GCs with lower metallicities appear further away from the galactic center, providing evidence that the dissolution time of GCs within galaxies is metallicity-dependent. This dependency is contingent upon a subsystem of BHs, BHSub, initially retained within the GC. The BHSub acts as an energy source, fueling the GC's stellar population through kinetic energy generated by fewbody BH encounters. However, additional factors such as the hierarchical build-up of galaxies and tidal interactions must also be considered to fully explain the observed radial metallicity trends.

The more massive and less expanded BHSub in metal-poor GCs fosters more intense few-body encounters, injecting more kinetic energy into the stellar population. This extra energy, coupled with the strong tidal field in the galactic central regions, accelerates the dissolution of lower-metallicity GCs on timescales shorter than the host galaxy's age. As the R_g increases, clusters experience a weaker galactic tidal field, reducing the impact of this excess internal energy on metal-poor GCs' evaporation rates, thus enabling their survival to the present day. In more massive galaxies, stronger tidal forces push surviving metal-poor GCs farther from the center, broadening the triangular depleted region in R_g -[Fe/H] space. Our analysis reveals a strong positive correlation between the morphology of the metal-poor GCs depleted region and the luminous mass (absolute magnitude; M_V) of the host galaxies, as quantified by a Pearson correlation coefficient of 0.9. More massive galaxies consistently exhibit more extended depleted regions. This correlation can serve as a novel method to estimate the galaxy distances.

These findings underscore the essential role of initial BH retention in the long-term evolution of GCs, suggesting limitations for scenarios in which BHs receive substantial natal kicks. In such models, the absence of a BHSub would eliminate the metallicity-dependence of cluster dissolution, and consequently fail to reproduce the triangular depleted region observed in the R_g –[Fe/H] diagram.

References

Alves-Brito, A., Hau, G. K. T., Forbes, D. A., et al. 2011, MNRAS, 417, 1823 Arca Sedda, M., Askar, A., & Giersz, M. 2018, MNRAS, 479, 4652 Askar, A., Arca Sedda, M., & Giersz, M. 2018, MNRAS, 478, 1844 Askar, A., Askar, A., Pasquato, M., & Giersz, M. 2019, MNRAS, 485, 5345 Atri, P., Miller-Jones, J. C. A., Bahramian, A., et al. 2019, MNRAS, 489, 3116 Banerjee, S. 2017, MNRAS, 467, 524 Banerjee, S. 2018, MNRAS, 481, 5123 Barnard, R., Garcia, M., Li, Z., Primini, F., & Murray, S. S. 2011, ApJ, 734, 79 Bassino, L. P., Richtler, T., & Dirsch, B. 2006, MNRAS, 367, 156 Baumgardt, H., Hilker, M., Sollima, A., & Bellini, A. 2019, MNRAS, 482, 5138 Baumgardt, H. & Kroupa, P. 2007, MNRAS, 380, 1589 Baumgardt, H. & Makino, J. 2003, MNRAS, 340, 227 Beasley, M. A., Bridges, T., Peng, E., et al. 2008, MNRAS, 386, 1443 Bekki, K., Forbes, D. A., Beasley, M. A., & Couch, W. J. 2002, MNRAS, 335, Belczynski, K., Bulik, T., Fryer, C. L., et al. 2010, ApJ, 714, 1217 Belczynski, K., Kalogera, V., Rasio, F. A., et al. 2008, ApJS, 174, 223

- Bica, E., Bonatto, C., Barbuy, B., & Ortolani, S. 2006, A&A, 450, 105 Bland-Hawthorn, J. & Gerhard, O. 2016, ARA&A, 54, 529
- Bonaca, A. & Price-Whelan, A. M. 2025, New A Rev., 100, 101713 Breen, P. G. & Heggie, D. C. 2013, MNRAS, 432, 2779

- Brüns, R. C. & Kroupa, P. 2012, A&A, 547, A65
- Castro-Ginard, A., Jordi, C., Luri, X., et al. 2018, A&A, 618, A59 Chatterjee, S., Rodriguez, C. L., & Rasio, F. A. 2017, ApJ, 834, 68
- Chattopadhyay, D., Hurley, J., Stevenson, S., & Raidani, A. 2022, MNRAS, 513,
- Chies-Santos, A. L., Larsen, S. S., Cantiello, M., et al. 2012, A&A, 539, A54
- Chomiuk, L., Strader, J., Maccarone, T. J., et al. 2013, ApJ, 777, 69 Côté, P., Marzke, R. O., West, M. J., & Minniti, D. 2000, ApJ, 533, 869
- Crnojević, D., Sand, D. J., Spekkens, K., et al. 2016, ApJ, 823, 19
- Dashwood Brown, C., Gandhi, P., & Zhao, Y. 2024, MNRAS, 527, L82
- de Vaucouleurs, G., de Vaucouleurs, A., Corwin, Herold G., J., et al. 1991, Third Reference Catalogue of Bright Galaxies
- Dickson, N., Smith, P. J., Hénault-Brunet, V., Gieles, M., & Baumgardt, H. 2024, MNRAS, 529, 331
- Forbes, D. A., Brodie, J. P., & Grillmair, C. J. 1997, AJ, 113, 1652
- Fryer, C. L., Belczynski, K., Wiktorowicz, G., et al. 2012, ApJ, 749, 91
- Galleti, S., Federici, L., Bellazzini, M., Fusi Pecci, F., & Macrina, S. 2004, A&A, 416, 917
- Ghasemi, S. M., Rostami-Shirazi, A., Khalaj, P., Zonoozi, A. H., & Haghi, H. 2024, MNRAS, 535, 1475
- Gieles, M., Athanassoula, E., & Portegies Zwart, S. F. 2007, MNRAS, 376, 809 Gieles, M., Erkal, D., Antonini, F., Balbinot, E., & Peñarrubia, J. 2021, Nature Astronomy, 5, 957
- Gieles, M. & Gnedin, O. Y. 2023, MNRAS, 522, 5340
- Gieles, M., Portegies Zwart, S. F., Baumgardt, H., et al. 2006, MNRAS, 371, 793
- Giersz, M., Askar, A., Wang, L., et al. 2019, MNRAS, 487, 2412
- Giesers, B., Dreizler, S., Husser, T.-O., et al. 2018, MNRAS, 475, L15
- Giesers, B., Kamann, S., Dreizler, S., et al. 2019, A&A, 632, A3
- Gnedin, O. Y., Lee, H. M., & Ostriker, J. P. 1999, ApJ, 522, 935
- Gnedin, O. Y. & Ostriker, J. P. 1997, ApJ, 474, 223
- Hansen, B. M. S., Kalirai, J. S., Anderson, J., et al. 2013, Nature, 500, 51
- Harris, W. E. 2001, in Saas-Fee Advanced Course 28: Star Clusters, ed. L. Labhardt & B. Binggeli, 223
- Harris, W. E. 2009, ApJ, 703, 939
- Harris, W. E. 2023, ApJS, 265, 9
- Hartman, K., Harris, W. E., Blakeslee, J. P., Ma, C.-P., & Greene, J. E. 2023, ApJ, 953, 154
- Heger, A., Fryer, C. L., Woosley, S. E., Langer, N., & Hartmann, D. H. 2003, ApJ, 591, 288
- Heggie, D. & Hut, P. 2003, The Gravitational Million-Body Problem: A Multidisciplinary Approach to Star Cluster Dynamics
- Iben, I. & Renzini, A. 1984, Phys. Rep., 105, 329
- Jordán, A. 2004, ApJ, 613, L117
- Komiyama, Y., Chiba, M., Tanaka, M., et al. 2018, ApJ, 853, 29
- Kremer, K., Chatterjee, S., Ye, C. S., Rodriguez, C. L., & Rasio, F. A. 2019, ApJ, 871, 38
- Kremer, K., Ye, C. S., Chatterjee, S., Rodriguez, C. L., & Rasio, F. A. 2018, ApJ,
- Kruijssen, J. M. D., Pfeffer, J. L., Chevance, M., et al. 2020, MNRAS, 498, 2472 Kruijssen, J. M. D., Pfeffer, J. L., Reina-Campos, M., Crain, R. A., & Bastian, N. 2019, MNRAS, 486, 3180
- Kundu, A. & Whitmore, B. C. 1998, AJ, 116, 2841 Law, D. R. & Majewski, S. R. 2010, ApJ, 718, 1128
- Li, Y., Mac Low, M.-M., & Klessen, R. S. 2004, ApJ, 614, L29
- Ma, J., Wu, Z.-Y., Zhang, T.-M., et al. 2013, Research in Astronomy and Astrophysics, 13, 399
- Maccarone, T. J., Kundu, A., Zepf, S. E., & Rhode, K. L. 2007, Nature, 445, 183 Mackey, A. D., Wilkinson, M. I., Davies, M. B., & Gilmore, G. F. 2007, MN-RAS, 379, L40
- Mackey, A. D., Wilkinson, M. I., Davies, M. B., & Gilmore, G. F. 2008, MN-RAS, 386, 65
- Malhan, K., Ibata, R. A., Sharma, S., et al. 2022, ApJ, 926, 107
- Mapelli, M. & Bressan, A. 2013, MNRAS, 430, 3120
- Marks, M. & Kroupa, P. 2012, A&A, 543, A8
- Marks, M., Kroupa, P., Dabringhausen, J., & Pawlowski, M. S. 2012, MNRAS,
- Massari, D., Koppelman, H. H., & Helmi, A. 2019, A&A, 630, L4
- Merritt, D., Milosavljević, M., Favata, M., Hughes, S. A., & Holz, D. E. 2004, ApJ, 607, L9
- Miller-Jones, J. C. A., Strader, J., Heinke, C. O., et al. 2015, MNRAS, 453, 3918 Morscher, M., Pattabiraman, B., Rodriguez, C., Rasio, F. A., & Umbreit, S. 2015, ApJ, 800, 9
- Nagarajan, P. & El-Badry, K. 2025, PASP, 137, 034203
- Naidu, R. P., Conroy, C., Bonaca, A., et al. 2020, ApJ, 901, 48
- Oppenheimer, J. R. & Snyder, H. 1939, Physical Review, 56, 455
- Peng, E. W., Jordán, A., Côté, P., et al. 2006, ApJ, 639, 95

- Peng, E. W., Jordán, A., Côté, P., et al. 2008, ApJ, 681, 197
- Peuten, M., Zocchi, A., Gieles, M., Gualandris, A., & Hénault-Brunet, V. 2016, MNRAS, 462, 2333
- Pfeffer, J., Kruijssen, J. M. D., Crain, R. A., & Bastian, N. 2018, MNRAS, 475, 4309
- Pota, V., Forbes, D. A., Romanowsky, A. J., et al. 2013, MNRAS, 428, 389 Rostami-Shirazi, A., Baumgardt, H., Zonoozi, A. H., Ghasemi, S. M., & Haghi, H. 2025a, MNRAS, 536, 1332
- Rostami-Shirazi, A., Haghi, H., Khalaj, P., Asl, A. F., & Hasani Zonoozi, A. 2022, MNRAS, 513, 3526
- Rostami-Shirazi, A., Haghi, H., Zonoozi, A. H., Farhani Asl, A., & Kroupa, P. 2024a, MNRAS, 531, 4166
- Rostami-Shirazi, A., Haghi, H., Zonoozi, A. H., & Kroupa, P. 2025b, ApJ, 989,
- Rostami-Shirazi, A., Khalaj, P., & Haghi, H. 2024b, MNRAS, 531, 2563 Rostami-Shirazi, A., Zonoozi, A. H., Haghi, H., & Rabiee, M. 2024c, MNRAS,
- 535, 3489 Saracino, S., Kamann, S., Guarcello, M. G., et al. 2022, MNRAS, 511, 2914
- Schuberth, Y., Richtler, T., Hilker, M., et al. 2010, A&A, 513, A52 Schulman, R. D., Glebbeek, E., & Sills, A. 2012, MNRAS, 420, 651
- Shanahan, R. L. & Gieles, M. 2015, MNRAS, 448, L94 Shih, I. C., Kundu, A., Maccarone, T. J., Zepf, S. E., & Joseph, T. D. 2010, ApJ,
- 721, 323
- Shishkovsky, L., Strader, J., Chomiuk, L., et al. 2018, ApJ, 855, 55
- Spitzer, L. S. 2014, in Dynamical Evolution of Globular Clusters (Princeton University Press)
- Strader, J., Chomiuk, L., Maccarone, T. J., Miller-Jones, J. C. A., & Seth, A. C. 2012a, Nature, 490, 71
- Strader, J., Fabbiano, G., Luo, B., et al. 2012b, ApJ, 760, 87
- Strader, J., Romanowsky, A. J., Brodie, J. P., et al. 2011, ApJS, 197, 33
- Tonini, C. 2013, ApJ, 762, 39
- Torniamenti, S., Gieles, M., Penoyre, Z., et al. 2023, MNRAS, 524, 1965 Vigna-Gómez, A., Willcox, R., Tamborra, I., et al. 2024, Phys. Rev. Lett., 132, 191403
- Vink, J. S. & de Koter, A. 2005, A&A, 442, 587
- Vink, J. S., de Koter, A., & Lamers, H. J. G. L. M. 2001, A&A, 369, 574 Wang, L. 2020, MNRAS, 491, 2413
- Weatherford, N. C., Chatterjee, S., Kremer, K., & Rasio, F. A. 2020, ApJ, 898,
- Weatherford, N. C., Chatterjee, S., Rodriguez, C. L., & Rasio, F. A. 2018, ApJ, 864, 13
- Woodley, K. A., Harris, W. E., Beasley, M. A., et al. 2007, AJ, 134, 494 Zhao, Y., Gandhi, P., Dashwood Brown, C., et al. 2023, MNRAS, 525, 1498 Zinn, R. 1985, ApJ, 293, 424

Appendix A: Galaxy sample and data sources

Properties of the studied galaxies, data sources for their GC systems, and statistical analyses evaluating the depletion of metal-poor GCs are summarized in Table A.1.

Table A.1. Properties of the studied galaxies and their GC systems.

Galaxy	M_V (mag)	\widetilde{P}_{DEP}	$\widetilde{\widetilde{P}}_{OUT}$	NND _{DEP}	NND _{OUT}	$p_{\mathrm{KS-DEP}}$	p _{KS-OUT}	p_{χ^2}	$p_{ m Poisson}$	R _{DEP} (kpc)
M 81 ²	$\frac{-21.20^{I}}{}$	7.88	1.20	0	0.48	0.00	0.80	0.12	0.00	2.22 ± 1.19
Milky Way ^{a 4 5}	-21.37^{3}	7.91	0.39	0	1.65	0.05	0.01	0.03	0.00	1.98 ± 1.25
M 31 ⁸	-21.61^{67}	17.04	0.66	0	1.40	0.12	0.87	0.08	0.00	3.62 ± 1.24
NGC 3258 ⁹	-21.95^9	5.12	1.09	0.46	0.98	0.01	0.89	0.00	0.00	5.06 ± 1.07
NGC 3268 ⁹	-21.95^9	4.67	1.20	0.27	0.97	0.17	0.36	0.02	0.00	6.01 ± 1.08
NGC 5322 ⁹	-22.00^{9}	3.80	0.95	0	1.11	0.22	0.02	0.22	0.08	5.00 ± 1.19
NGC 5128 ¹¹ 12	$-22.01^{6\ 10}$	6.52	1.23	0.55	0.97	0.00	0.07	0.22	0.00	4.12 ± 1.28
NGC 1407 ⁹	-22.04^9	5.17	2.02	0.30	0.71	0.04	0.06	0.03	0.00	5.12 ± 1.14
NGC 7626 ⁹	-22.06^9	2.71	1.03	0.67	0.98	0.04	0.30	0.36	0.00	6.24 ± 1.09
NGC 5557 ⁹	-22.33^{9}	10.50	1.26	0	0.88	0.04	0.07	0.41	0.00	5.75 ± 1.09
$M 104^{13}$	-22.45^2	6.37	0.73	0	1.45	0.07	0.48	0.17	0.00	4.82 ± 1.19
NGC 1278 ⁹	-22.54^{6} 9	3.04	0.60	0.57	1.34	0.07	0.50	0.05	0.00	16.75 ± 1.14
NGC 1600 ¹⁴	-22.60^{6}	6.15	2.42	0.39	0.67	0.00	0.00	0.00	0.00	13.15 ± 1.05
NGC 4914 ¹⁴	-22.70^6	20.51	4.55	0	0.43	0.02	0.09	0.01	0.00	15.62 ± 1.10
NGC 1275 ⁹	-22.74^{9}	6.88	0.98	0.28	0.95	0.00	0.70	0.01	0.00	14.71 ± 1.09
NGC 533 ¹⁴	-22.80^{6}	10.35	2.28	0.25	0.48	0.00	0.11	0.00	0.00	14.43 ± 1.06
NGC 777 ¹⁴	-22.80^{6}	30.63	2.48	0.35	0.65	0.00	0.00	0.00	0.00	15.75 ± 1.06
NGC 57 ¹⁴	-22.80^6	6.99	1.36	0.60	0.86	0.00	0.05	0.00	0.00	16.93 ± 1.10
NGC 1132 ⁹	-22.87^9	3.87	0.91	0.45	1.06	0.00	0.89	0.00	0.00	13.00 ± 1.08
NGC 3842 ¹⁴	-22.90^{6}	7.20	1.51	0.22	0.80	0.00	0.00	0.00	0.00	15.93 ± 1.05
NGC 1016 ¹⁴	-22.90^{6}	8.60	2.02	0.56	0.73	0.00	0.12	0.00	0.00	19.01 ± 1.11
UGC 10143 ⁹	-22.90^{9}	3.13	0.83	0.67	1.10	0.04	0.26	0.09	0.00	27.16 ± 1.08
ESO 509-G008 ⁹	-23.04^9	9.46	0.83	0.17	1.26	0.00	0.79	0.00	0.00	19.35 ± 1.06
NGC 1272 ⁹	-23.09^9	5.54	0.81	0.51	1.15	0.00	0.95	0.00	0.00	22.17 ± 1.08
NGC 410 ¹⁴	-23.10^{6}	11.67	1.81	0	0.56	0.00	0.63	0.26	0.00	14.70 ± 1.08
NGC 741 ¹⁴	-23.10^{6}	11.73	1.69	0	0.76	0.01	0.01	0.31	0.00	17.16 ± 1.12
NGC 2340 ¹⁴	-23.10^{6}	5.95	1.61	0.40	0.53	0.00	0.89	0.19	0.00	24.83 ± 1.11
NGC 4839 ¹⁴	-23.20^{6}	10.07	1.81	0.16	0.84	0.00	0.00	0.00	0.00	16.19 ± 1.07
UGC 9799 ⁹	-23.20^9	5.44	0.98	0.44	1.02	0.00	0.81	0.00	0.00	22.57 ± 1.08
NGC 4073 ¹⁴	-23.30^{6}	10.12	1.89	0.12	0.76	0.00	0.00	0.03	0.00	15.33 ± 1.06
NGC 3158 ¹⁴	-23.30^{6}	4.64	1.84	0.23	0.79	0.00	0.00	0.01	0.00	16.01 ± 1.05
NGC 4874 ⁹	-23.37^9	3.70	0.92	0.50	1.04	0.01	0.90	0.00	0.00	16.38 ± 1.06
NGC 7720 ⁹	-23.39^9	3.70	0.83	0.61	0.99	0.00	0.75	0.00	0.00	20.54 ± 1.07
ESO 306-G017 ⁹	-23.63^9	4.63	1.01	0.65	1.05	0.00	0.19	0.00	0.00	29.67 ± 1.08
NGC 6166 ⁹	-23.65^9	3.61	0.84	0.63	1.07	0.00	0.56	0.01	0.00	21.75 ± 1.08
NGC 4889 ⁹	-23.69^9	7.27	0.84	0.47	1.06	0.04	0.26	0.00	0.00	15.91 ± 1.08
ESO 444-G046 ⁹	-23.81^9	2.14	1.07	0.65	1.02	0.07	0.01	0.00	0.00	20.84 ± 1.05
Mean		7.69	1.36	0.33	0.93	0.03	0.36	0.07	0.00	

Notes. Columns: (1) galaxy names and the associated references for their GC system data, (2) integrated V-band absolute magnitudes (M_V) , (3) total probability ratio in the depleted region (P_{DEP}) , (4) total probability ratio in the outer region (P_{OUT}) , (5) mean nearest neighbor distance ratio in the depleted region (NND_{DEP}) , (6) mean nearest neighbor distance ratio in the outer region (NND_{OUT}) , (7) p-value from the Kolmogorov-Smirnov (K-S) test for the inner regions (p_{KS-DEP}) , (8) p-value from the K-S test for the outer regions (p_{KS-OUT}) , (9) p-value from the chi-square test in the depleted region (p_{χ^2}) , (10) Poisson probability for the depleted region $(p_{Poisson})$, and (11) mean depopulation radius (R_{DEP}) with its standard deviation, obtained from 1000 CDF resampling.

References: (1) Brüns & Kroupa (2012); (2) Ma et al. (2013); (3) Bland-Hawthorn & Gerhard (2016); (4) Kruijssen et al. (2019); (5) Baumgardt et al. (2019); (6) de Vaucouleurs et al. (1991); (7) Komiyama et al. (2018); (8) Galleti et al. (2004); (9) Harris (2023); (10) Crnojević et al. (2016); (11) Beasley et al. (2008); (12) Woodley et al. (2007); (13) Alves-Brito et al. (2011); (14) Hartman et al. (2023) . (a) For the Milky Way (MW) analysis, the semi-major axis measurements of GCs were employed instead of R_g .